

**Structural and spectroscopic properties of the polar antiferromagnet Ni<sub>2</sub>MnTeO<sub>6</sub>**

Maria Retuerto,<sup>1,2</sup> Stella Skiadopoulou,<sup>3,4</sup> Fedir Borodavka,<sup>3</sup> Christelle Kadlec,<sup>3</sup> Filip Kadlec,<sup>3</sup> Jan Prokleška,<sup>5</sup> Zheng Deng,<sup>1</sup> Jose A. Alonso,<sup>6</sup> Maria T. Fernandez-Diaz,<sup>7</sup> Felix O. Saouma,<sup>8</sup> Joon I. Jang,<sup>9</sup> Dominik Legut,<sup>4</sup> Stanislav Kamba,<sup>3</sup> and Martha Greenblatt<sup>1,\*</sup>

<sup>1</sup>*Department of Chemistry and Chemical Biology, Rutgers, The State University of New Jersey, 610 Taylor Road, Piscataway, New Jersey 08854, USA*

<sup>2</sup>*Grupo de Energía y Química Sostenibles, Instituto de Catálisis y Petroleoquímica, CSIC. C/Marie Curie 2, 28049, Madrid, Spain*

<sup>3</sup>*Institute of Physics, Czech Academy of Sciences, Na Slovance 2, 18221 Prague 8, Czech Republic*

<sup>4</sup>*IT4Innovations Center, VSB Technical University Ostrava, 17 listopadu 15, CZ-708 33 Ostrava-Poruba, Czech Republic*

<sup>5</sup>*Department of Condensed Matter Physics, Faculty of Mathematics and Physics, Charles University, Ke Karlovu 5, 121 16 Prague 2, Czech Republic*

<sup>6</sup>*Instituto de Ciencia de Materiales de Madrid, CSIC, Cantoblanco, E-28049 Madrid, Spain*

<sup>7</sup>*Institut Laue Langevin, BP 156X, Grenoble F-38042, France*

<sup>8</sup>*Kaimosi Friends University College, P.O. Box 385, Kaimosi-50309, Kenya*

<sup>9</sup>*Department of Physics, Sogang University, 35 Baekbeom-ro, Mapo-gu, Seoul 04107, South Korea*

 (Received 5 December 2017; revised manuscript received 14 March 2018; published 23 April 2018)

We present a structural and spectroscopic study of the compound Ni<sub>2</sub>MnTeO<sub>6</sub>, closely related to the polar antiferromagnet Ni<sub>3</sub>TeO<sub>6</sub> known to show a colossal magnetoelectric effect and pronounced elementary magnetoelectric excitations. We prepared single crystals and polycrystalline samples of Ni<sub>2</sub>MnTeO<sub>6</sub> showing the same polar structure as Ni<sub>3</sub>TeO<sub>6</sub> from room temperature down to 4 K with the *R3* space-group symmetry. Magnetic and dielectric measurements have indicated an antiferromagnetic phase transition at  $T_N \approx 70$  K, almost 20 K higher than that of Ni<sub>3</sub>TeO<sub>6</sub>. Extensive infrared, Raman, and terahertz spectroscopy experiments were employed for investigating lattice and spin excitations, revealing all phonons predicted by the factor group analysis. Terahertz spectra below  $T_N$  reveal one new excitation, which is strongly influenced by external magnetic field, thus assigned to a magnon.

DOI: [10.1103/PhysRevB.97.144418](https://doi.org/10.1103/PhysRevB.97.144418)

**I. INTRODUCTION**

In pursuit of multiferroic compounds with crystal structure other than that of the perovskites, the corundum-related (Al<sub>2</sub>O<sub>3</sub>) family A<sub>2</sub>BB'O<sub>6</sub> scores a success among the magnetic systems [1–11] and lately, due to the colossal magnetoelectric effect in the polar antiferromagnet Ni<sub>3</sub>TeO<sub>6</sub>, the multiferroic community [12–16]. In the above structural formula, A is usually a small diamagnetic or paramagnetic divalent cation, B is usually a divalent or trivalent transition-metal cation, and B' is usually a pentavalent or hexavalent transition metal or a diamagnetic cation (e.g., Sb or Te).

During the 1980s, a few studies on corundum- and cryolite-related (a-Na<sub>3</sub>AlF<sub>6</sub>) compounds suggested ferroelectric (FE) properties for a series of M<sub>3</sub>TeO<sub>6</sub> compounds, with M corresponding to paramagnetic cations, and the reported Curie temperatures around 500 K [1,2]. However, no evidence of noncentrosymmetric structure for any of the above compounds at room temperature was reported ever since, except for Ni<sub>3</sub>TeO<sub>6</sub>. Thus, Mg<sub>3</sub>TeO<sub>6</sub> [17] and Mn<sub>3</sub>TeO<sub>6</sub> [6] crystallize in the rhombohedral  $R\bar{3}$  space group, Cd<sub>3</sub>TeO<sub>6</sub> [18] and Ca<sub>3</sub>TeO<sub>6</sub> [19] crystallize in the monoclinic  $P2_1/n$  space group, Co<sub>3</sub>TeO<sub>6</sub> crystallizes in the monoclinic  $C2/c$  [20] space group, and Cu<sub>3</sub>TeO<sub>6</sub> crystallizes in the cubic  $Ia\bar{3}$  [21]

space group. To date, Ni<sub>3</sub>TeO<sub>6</sub> and (Mn<sub>0.2</sub>Ni<sub>0.8</sub>)<sub>3</sub>TeO<sub>6</sub> are the only reported compounds without inversion symmetry [8]. The Ni<sub>3-x</sub>Mn<sub>x</sub>TeO<sub>6</sub> system shows the *R3* space group at room temperature, and, interestingly, it displays an antiferromagnetic (AFM) transition temperature of  $T_N = 67$  K [8], higher than that in Ni<sub>3</sub>TeO<sub>6</sub>. A further increase in  $T_N$  upon increasing  $x$  was suggested by Mathieu *et al.* [8] in view of an expected stabilization of the *R3* space group.

Aiming at enhancing the critical temperature, Ni<sub>2</sub>MnTeO<sub>6</sub> was synthesized in the form of single crystals and ceramics; their magnetic and dielectric properties were studied, together with lattice and spin dynamics. Since Ni<sub>3</sub>TeO<sub>6</sub> exhibits a strong magnetoelectric coupling which activates electromagnons in terahertz and Raman spectra [15], we wanted to check for the presence of such spin excitations also in Ni<sub>2</sub>MnTeO<sub>6</sub>. The increase in  $T_N$  predicted by Mathieu *et al.* [8] was confirmed, since Ni<sub>2</sub>MnTeO<sub>6</sub> exhibits an AFM transition at  $T_N \sim 70$  K. In addition, the terahertz spectra unveil a spin excitation below  $T_N$ .

**II. EXPERIMENTAL DETAILS**

Polycrystalline Ni<sub>2</sub>MnTeO<sub>6</sub> was prepared from stoichiometric amounts of analytical grade NiO, TeO<sub>2</sub>, and MnCO<sub>3</sub>. The mixture was heated in a tubular furnace under oxygen flux at 800 °C with intermediate grindings between 700 and 800 °C. Single crystals were prepared by the flux method in the

\*Corresponding author: greenbla@chem.rutgers.edu

following steps:  $\text{Ni}_2\text{MnTeO}_6 : \text{V}_2\text{O}_5 : \text{TeO}_2 : \text{NaCl} : \text{KCl}$  in a molar ratio of 1:5:10:10:5 was kept for two days at  $800^\circ\text{C}$  and then cooled down to  $600^\circ\text{C}$  during three days. Plate-shaped green crystals with lateral dimensions of less than 1 mm were obtained. The structure and purity of the polycrystalline powders were determined by powder x-ray diffraction (XRD) ( $\text{Cu } K_\alpha$ ,  $\lambda = 1.5406 \text{ \AA}$ ) and energy dispersive spectroscopy (EDS, x-ray microanalyzer JXA-733 Superprobe). For structural refinements, powder neutron diffraction (PND) was performed. PND was collected at the Institute Laue-Langevin, Grenoble. The data at room temperature were collected in the D2B High Resolution instrument ( $\lambda = 1.5940 \text{ \AA}$ ). For the determination of the magnetic structure between 5 and 100 K we used the D20 ( $\lambda = 2.410 \text{ \AA}$ ) instrument. Diffraction data analysis by Rietveld refinement [22] was performed with the Fullprof software [23]. The structure of the single crystals was determined by single-crystal x-ray data collected on a Bruker Smart APEX CCD diffractometer with graphite-monochromatized  $\text{Mo } K_\alpha$  radiation ( $\lambda = 0.71073 \text{ \AA}$ ) at 100 K. Magnetic measurements of the single crystals were performed on a Quantum Design superconducting quantum interference device system, whereas those of polycrystalline samples utilized the ACMS (ac Magnetic Studies, extraction magnetometer) and VSM (Vibrating Sample Magnetometer) options of the Physical Property Measurement System (PPMS) apparatus (Quantum Design) in fields up to 14 T and temperatures down to 2 K.

Near-normal incidence IR reflectivity spectra of the  $\text{Ni}_2\text{MnTeO}_6$  ceramics were measured by a Fourier-transform IR spectrometer Bruker IFS 113v in the frequency range of  $20\text{--}3000 \text{ cm}^{-1}$  ( $0.6\text{--}90 \text{ THz}$ ) at room temperature; for the low-temperature measurements, an Optistat optical cryostat (Oxford Instruments) with polyethylene windows was used; their transparency reduced the spectral range to  $20\text{--}650 \text{ cm}^{-1}$ . A pyroelectric deuterated triglycine sulfate detector was used for the room-temperature measurements, whereas a He-cooled

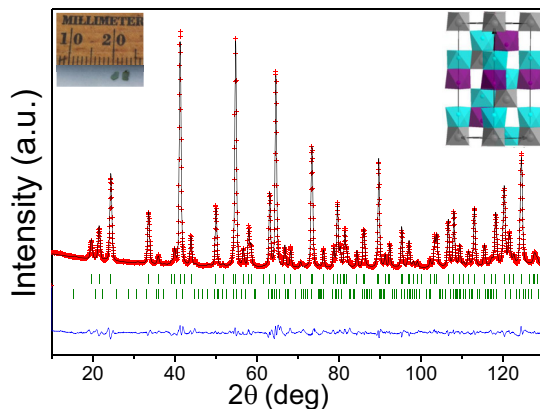


FIG. 1. Room temperature PND pattern of  $\text{Ni}_2\text{MnTeO}_6$ . The lower row of Bragg reflections (green lines) represents an impurity of  $\text{Mn}_3\text{TeO}_6$  amounting to 3%. Left inset: Photograph of the  $\text{Ni}_2\text{MnTeO}_6$  single crystals. Right inset: Schematic representation of the crystal structure: cyan,  $\text{NiO}_6$  octahedra; purple,  $\text{MnO}_6$  octahedra; and gray,  $\text{TeO}_6$  octahedra. The displacements of the atoms from the octahedral center can be seen.

( $T = 1.6 \text{ K}$ ) Si bolometer was used for the low-temperature measurements down to 7 K.

Terahertz measurements from  $3$  to  $60 \text{ cm}^{-1}$  ( $0.09\text{--}1.8 \text{ THz}$ ) were performed in the transmission geometry with a custom-made time-domain terahertz spectrometer. Here, a femtosecond Ti:sapphire laser oscillator (Coherent, Mira) produces a train of femtosecond pulses, which generate linearly polarized broadband terahertz pulses radiated by a photoconducting switch TeraSED (Giga-Optics). A gated detection scheme based on electro-optic sampling with a 1-mm-thick [110] ZnTe crystal as a sensor allows one to measure the time profile of the electric field of the transmitted terahertz pulse. An Oxford Instruments Optistat optical cryostat with mylar windows was used for low-temperature measurements. Terahertz experiments in an external magnetic field  $H_{\text{ext}} \leq 7 \text{ T}$  were performed with an Oxford Instruments Spectromag cryostat in the Voigt configuration, where the electric component of the terahertz radiation  $E_{\text{THz}}$  was set parallel and perpendicular to  $H_{\text{ext}}$ .

The IR reflectivity and terahertz complex permittivity spectra were fitted assuming a sum of  $N$  independent damped harmonic oscillators, expressed as [24]

$$\varepsilon^*(\omega) = \varepsilon_\infty + \sum_{j=1}^N \frac{\Delta\varepsilon_j \omega_{\text{TO}j}^2}{\omega_{\text{TO}j}^2 - \omega^2 + i\omega\gamma_{\text{TO}j}} \quad (1)$$

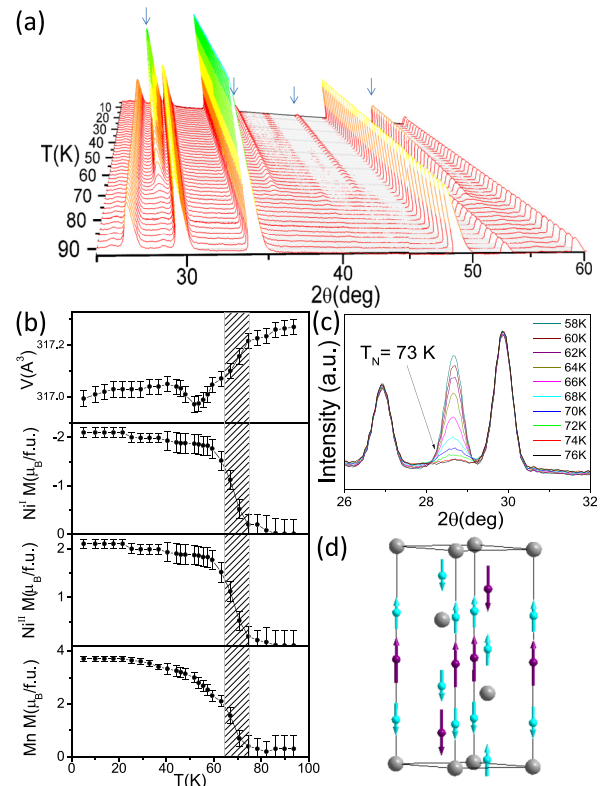


FIG. 2. (a) Thermal evolution of the PND pattern of polycrystalline  $\text{Ni}_2\text{MnTeO}_6$ , showing the peaks related to the AFM transition at  $\sim 70 \text{ K}$ . (b) Temperature dependence of the unit-cell volume and magnetic moments per magnetic cation. (c) Prominent magnetic transition at 73 K, as seen by the evolution of the PND peak. (d) Schematic representation of the AFM configuration (the magnetic unit cell is larger) (purple, Mn; cyan, Ni).

where  $\Delta\epsilon_j$  is the dielectric strength of the  $j$ th mode,  $\omega_{TOj}$  are the frequencies of the  $j$ th transverse optical (TO) phonons, and  $\gamma_{TOj}$  are the corresponding damping constants.  $\epsilon_\infty$  is the high-frequency (electronic) contribution to the permittivity, determined from the room-temperature frequency-independent reflectivity tail above the phonon frequencies. The reflectivity  $R(\omega)$  is related to the complex dielectric function  $\epsilon^*(\omega)$  by

$$R(\omega) = \left| \frac{\sqrt{\epsilon^*} - 1}{\sqrt{\epsilon^*} + 1} \right|^2. \quad (2)$$

For Raman studies of single crystals, a Renishaw RM 1000 Micro-Raman spectrometer with Bragg filters was used, equipped with an Oxford Instruments Microstat continuous-flow optical He cryostat. The experiments were performed in the backscattering geometry in the 5–1800-cm<sup>-1</sup> range. An Ar<sup>+</sup>-ion laser operating at 514.5 nm was used. The spectra were carefully fitted with a sum of independent damped harmonic oscillators multiplied by the corresponding Stokes temperature factor [25].

Spin-polarized density functional theory calculations were conducted, implementing the projector-augmented-wave formalism to describe the electron-ion interactions, and the gener-

alized gradient approximation (GGA) parametrized by Pedrew, Burke, and Ernzerhof for the exchange-correlation potential [26,27]. To account for the correct AFM order, the unit cell was doubled along the  $c$  axis and sampled by a  $5 \times 5 \times 2$  grid. The lattice dynamics calculations were used within the PHONOPY code, employing calculated Hellman Feynman forces, and using  $2 \times 2 \times 2$  supercell with 60 displacements of 0.01 Å. Additional on-site Coulomb repulsion interactions were considered concurrently, within the rotationally invariant form of the GGA+ $U$  approach [28], where the localized 3d electrons experience a spin- and orbital-dependent potential ( $U$ ) and the exchange interaction  $J$ , while the other orbitals are delocalized and treated by the conventional GGA approximation.

### III. RESULTS AND DISCUSSION

#### A. Structural characterization

Based on the room-temperature PND (Fig. 1) and XRD characterization, we determined that the structure of Ni<sub>2</sub>MnTeO<sub>6</sub> is analogous to that of Ni<sub>3</sub>TeO<sub>6</sub> [rhombohedral, space group  $R\bar{3}$  (no. 146),  $Z = 3$ ], which can be viewed as a A<sub>2</sub>BB'O<sub>6</sub>-type corundum derivative. The structure contains

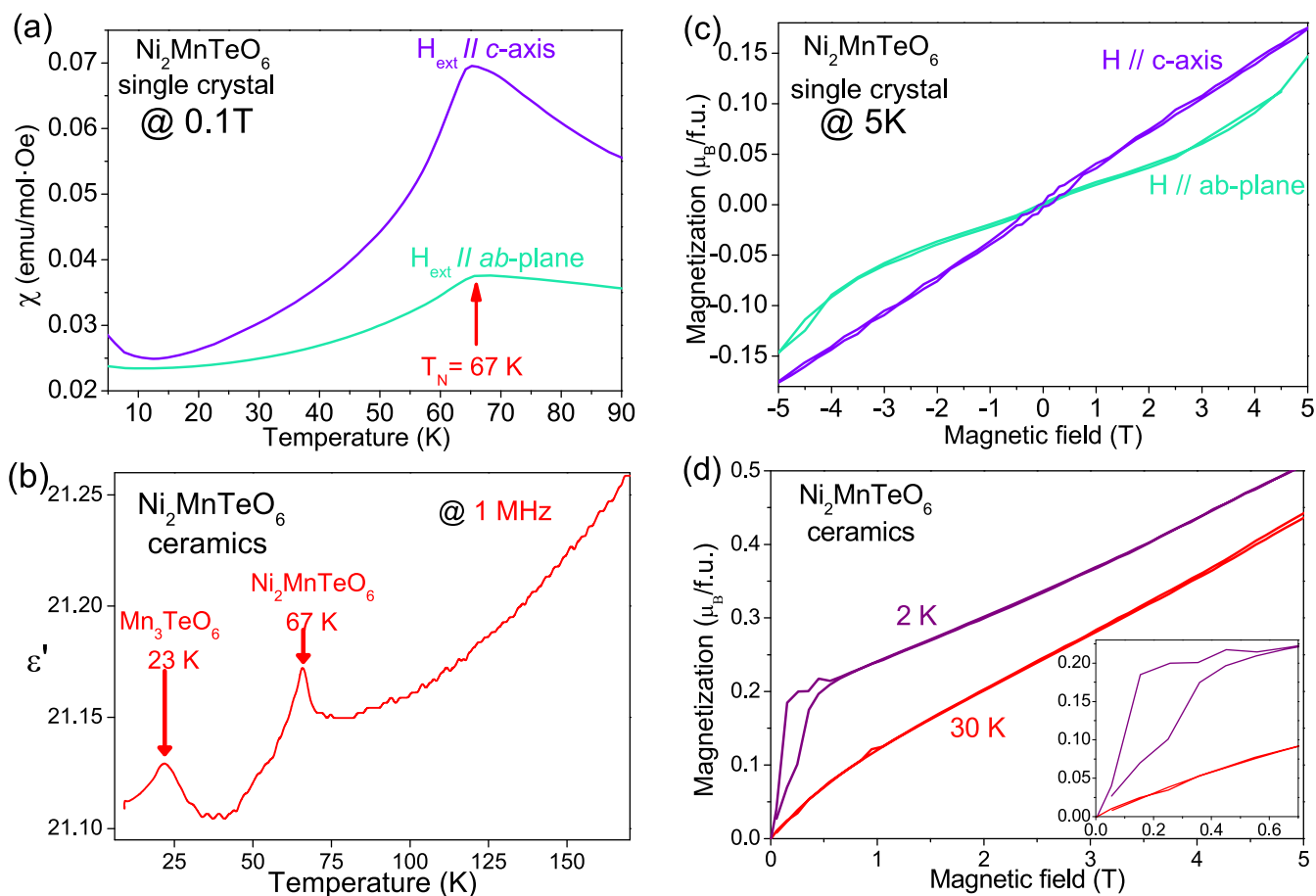


FIG. 3. (a) Temperature dependence of magnetic susceptibility of the Ni<sub>2</sub>MnTeO<sub>6</sub> single crystal at 0.1 T with two distinct orientations:  $H_{\text{ext}} \parallel c$  and  $H_{\text{ext}} \perp c$ ; the anomaly appears at  $\sim 67$  K. (b) Temperature dependence of the permittivity of Ni<sub>2</sub>MnTeO<sub>6</sub> ceramics, recorded at 1 MHz; the anomaly occurring around 67 K is due to the spin-order-induced change of polar dielectric structure, whereas the one anomaly at 23 K is probably due to a FE phase transition in the secondary phase of Mn<sub>3</sub>TeO<sub>6</sub>. (c, d) Magnetic-field dependences of magnetization in the single crystal and ceramics, respectively. In the single crystal, a spin-flop transition occurs at  $\sim 4.5$  T, which is not observed in the ceramics. The inset of (d) shows low-magnetic-field hysteric behavior in the ceramics, most probably due to the Mn<sub>3</sub>TeO<sub>6</sub> secondary phase.

two crystallographically distinct Ni atoms at the A sites, denoted here as Ni<sup>I</sup> and Ni<sup>II</sup>, ordered Mn and Te on both B sites, and two independent oxygen atoms (for details see Tables S1 and S2 in Supplemental Material [29]). XRD on single crystals revealed slightly different lattice parameters, which can be explained by a small difference between Ni/Mn ratios in crystals and ceramics. The structure is formed by layers of edge-sharing TeO<sub>6</sub> and Ni<sup>I</sup>O<sub>6</sub> octahedra in the *ab* plane; these layers alternate with those containing edge-sharing MnO<sub>6</sub> and Ni<sup>II</sup>O<sub>6</sub> octahedra. The layers are connected along the *c* axis by face-sharing dimers of TeO<sub>6</sub>/Ni<sup>I</sup>O<sub>6</sub> and MnO<sub>6</sub>/Ni<sup>II</sup>O<sub>6</sub> (see the inset of Fig. 1). The noncentrosymmetry of the Ni<sub>2</sub>MnTeO<sub>6</sub> structure was supported by second harmonic generation measurements (see Fig. S2 in Supplemental Material [29]).

Due to electrostatic repulsion, the cations inside the face-sharing octahedra are displaced from their centers along the *c* direction, moving closer to the octahedral vacancies and farther away from the other cation in the dimer. This gives rise to three long and three short octahedral separations. This effect is more pronounced in Ni<sub>2</sub>MnTeO<sub>6</sub> than in Ni<sub>3</sub>TeO<sub>6</sub> [30], and it is analogous to that in the isostructural Mn<sub>2</sub>FeWO<sub>6</sub> [16].

**B. Magnetic structure**

In order to determine the magnetic structure, PND at low temperatures was measured. The temperature dependences of the diffraction pattern, unit-cell volume, and magnetic moments are shown in Figs. 2(a) and 2(b). The magnetic transition is clearly observed at  $T_N \approx 70$  K [Fig. 2(c)], nearly 20 K higher than in Ni<sub>3</sub>TeO<sub>6</sub>. The magnetic structure [Fig. 2(d)] is AFM,

characterized by a propagation vector  $\mathbf{k} = (003/2)$ , and it consists of spins ferromagnetically ordered in adjacent *ab* planes, pairwise alternately pointing parallel and antiparallel along the *c* direction.

The magnetic moments at Ni<sup>I</sup>, Ni<sup>II</sup>, and Mn sites at 5 K were refined as 2.1(2)  $\mu_B$ /f.u. for Ni and 3.7(3)  $\mu_B$ /f.u. for Mn. The moments at the Ni positions are slightly larger than those expected for the Ni<sup>2+</sup> spin state  $S = 1$ , which can be explained by the disorder with Mn<sup>2+</sup>, expected to exhibit a spin state of  $S = 5/2$ . The same is true of Mn moments, that are slightly smaller than expected due to the partial disorder.

Employing first-principles calculations, we have determined the structural geometry with the AFM order as depicted in Fig. 2(d). The calculated hexagonal lattice parameters of  $a = 5.21386 \text{ \AA}$  and  $c = 14.17241 \text{ \AA}$  correspond to a less than 1% higher volume value than the experimental one (see Table S1 in Supplemental Material [29]). Within the GGA+*U* approach,  $U_{\text{eff}} = U - J$  is only meaningful where  $U_{\text{eff}} = 7 \text{ eV}$  for both Ni and Mn sites, yielding the Ni and Mn magnetic moments 1.8 and 4.8  $\mu_B$ , respectively. These values lie close to the previously reported experimental ones for Ni (2  $\mu_B$ ) and Mn (3–6  $\mu_B$ ), in the Ni<sub>3</sub>TeO<sub>6</sub> [31] and Mn<sub>3</sub>TeO<sub>6</sub> [6] compounds, respectively.

**C. Magnetic and dielectric properties**

The temperature dependence of the magnetic susceptibility measurements for Ni<sub>2</sub>MnTeO<sub>6</sub> single crystal is displayed in Fig. 3(a), for two orientations of the magnetic field:  $\mathbf{H}_{\text{ext}} \parallel c$  and  $\mathbf{H}_{\text{ext}} \perp c$ . The AFM transition occurs at  $\sim 67$  K, and it is

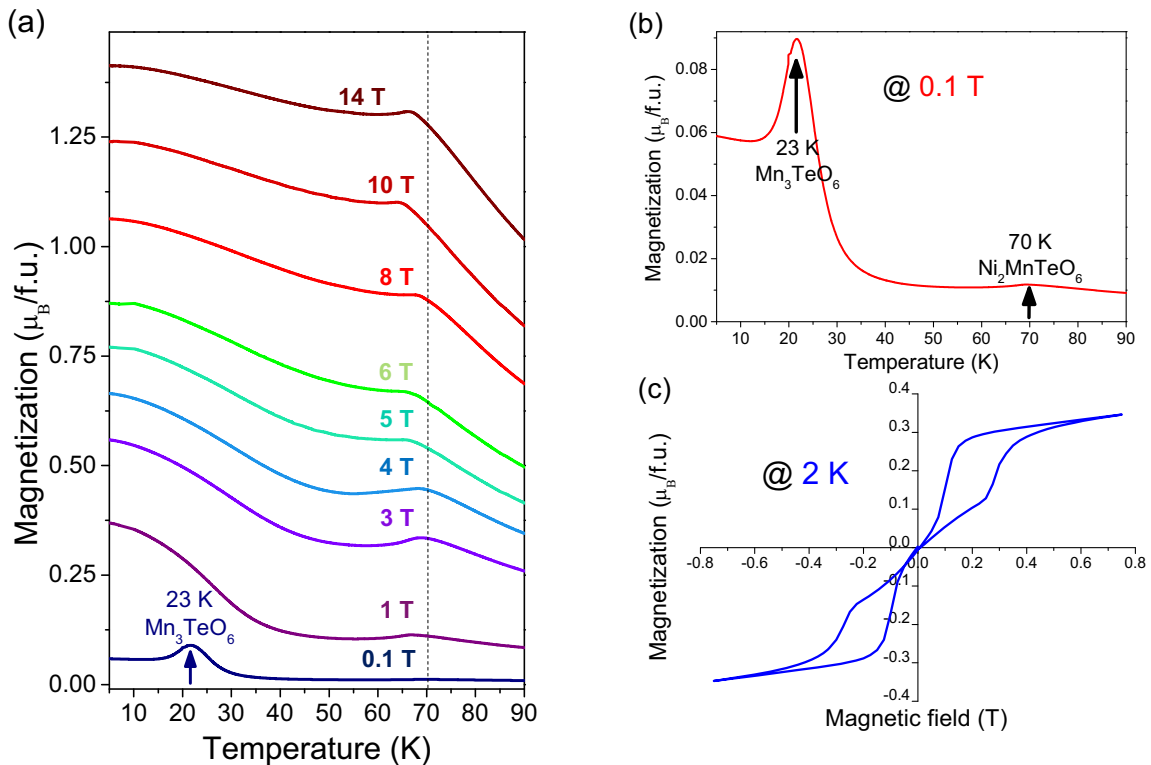


FIG. 4. Temperature dependence of magnetization of Ni<sub>2</sub>MnTeO<sub>6</sub> ceramics (a) up to 14 T and (b) at 0.1 T. Two conspicuous AFM transition temperatures of 23 and 70 K attest the presence of two distinct phases, Mn<sub>3</sub>TeO<sub>6</sub> and Ni<sub>2</sub>MnTeO<sub>6</sub>, respectively. (c) A hysteretic magnetic-field dependence of magnetization of Ni<sub>2</sub>MnTeO<sub>6</sub> ceramics, recorded at low magnetic fields of up to 0.8 T and at 2 K.

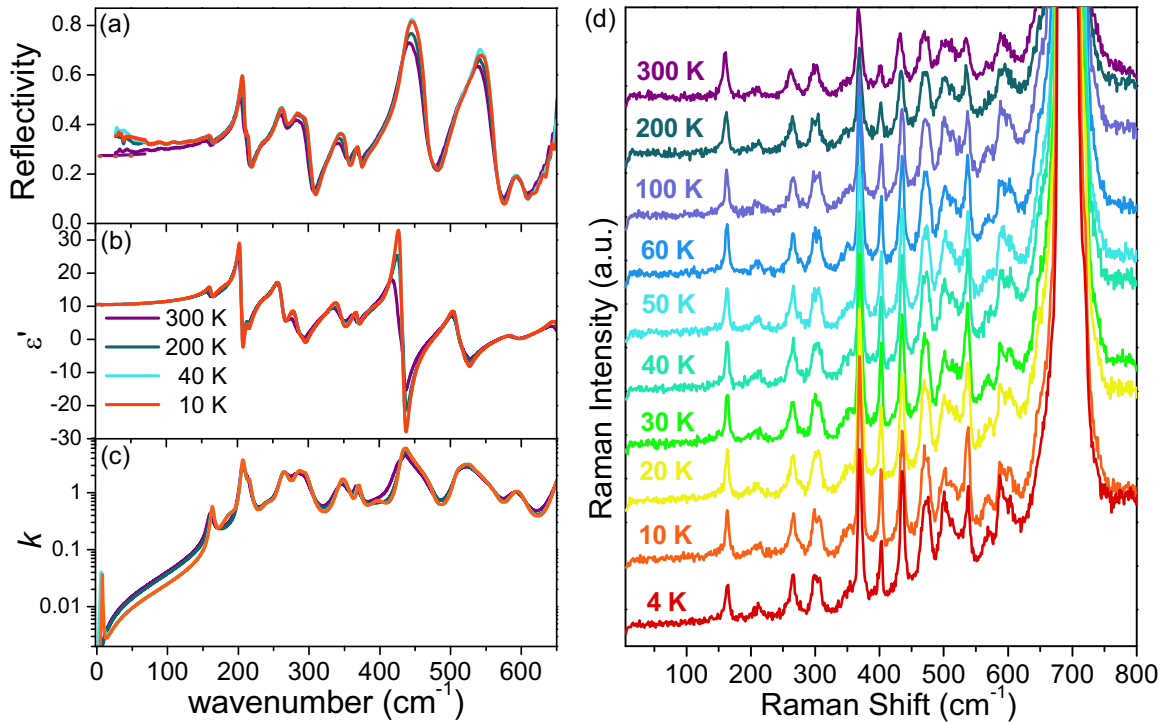


FIG. 5. (a) IR reflectivity spectra measured at selected temperatures from 10 to 300 K. (b) Real part of permittivity and (c) imaginary part of the index of refraction, as obtained from the fits or IR reflectivity and experimental terahertz spectra using Eqs. (1) and (2). (d) Raman cross-polarized spectra for different temperatures from 4 to 300 K.

markedly stronger in the susceptibility along  $c$ , as expected from the magnetic structure (Fig. 2). The discrepancy between the values of the Néel temperature, 73 K from PND data and 67 K from the magnetic measurements, can be ascribed to the different experimental techniques, and to the use of different samples (polycrystalline in the former and single crystalline in the latter case) with slightly different Ni/Mn ratios. Figure 3(b) shows the temperature dependence of permittivity in the ceramics measured at 1 MHz. Since the magnetic structure was shown to be collinear with the  $c$  axis, the decrease in  $\chi$  observed below  $T_N$  for  $\mathbf{H}_{\text{ext}} \perp c$  is probably an artifact of a partial sample misalignment. The dielectric anomaly appearing at 67 K, at the AFM transition, indicates an interplay between the magnetic and polar characters (i.e., change in the electric polarization) of the phase transition. An additional dielectric anomaly is clearly seen at 23 K. This temperature corresponds to a phase transition in  $\text{Mn}_3\text{TeO}_6$  which is AFM and probably FE [6]. The  $\text{Mn}_3\text{TeO}_6$  secondary phase, amounting to  $\sim 3\%$ , is observed by PND (Fig. 1). According to literature,  $\text{Mn}_3\text{TeO}_6$  should conserve the noncentrosymmetric rhombohedral  $R\bar{3}$  space group down to 5 K [6]. However, Zhao *et al.* [32] reported a FE phase transition a few Kelvin below the AFM one, at around 21 K. The FE distortion is so small that it was not detected in previously published PND studies [6], and Ivanov *et al.* [33] attempted to perform a more detailed structural analysis in order to explain this intriguing behavior, however with no success. Note that for most spin-order induced FEs the FE distortions were not resolved in diffraction experiments, but only in dielectric measurements, because the FE distortions are usually very small [34].

In Figures 3(c) and 3(d), the magnetic-field dependences of the magnetization for both the single crystal (c) and ceramics (d) are presented. The single-crystal experiment was done at 5 K and for two magnetic-field orientations:  $\mathbf{H}_{\text{ext}} \parallel c$  axis and  $\mathbf{H}_{\text{ext}} \parallel ab$  plane, with  $\mu_0 H$  of up to 5 T. The ceramic sample was measured at 2 and 30 K, up to 14 T, however here we present data only up to 5 T. The single crystal shows an easy-axis magnetization along  $c$ , and a nonhysteretic spin-flop transition around 4 T, resembling its unsubstituted counterpart  $\text{Ni}_3\text{TeO}_6$ , which manifests a nonhysteretic spin-flop transition at  $\sim 8$  T [12]. Curiously, the ceramic sample only presents a very weak bend in the magnetization curve at  $\sim 4.5$  T, whereas a hysteretic behavior, possibly of a FM origin, appears at very low fields, below 0.3 T [see inset of Fig. 3(d)]. We attribute this hysteresis to the secondary  $\text{Mn}_3\text{TeO}_6$  phase in the ceramics sample. The secondary phase is also responsible for the higher magnetization of ceramics than that of the crystal, because  $\text{Mn}_3\text{TeO}_6$  has a susceptibility higher than  $\text{Ni}_2\text{MnTeO}_6$  [6].

Figure 4(a) presents the temperature dependences of magnetization for the polycrystalline  $\text{Ni}_2\text{MnTeO}_6$  at various values of applied magnetic field. For any value of  $H$ , the magnetic transition takes place at  $\sim 70$  K, in agreement with the PND results.

A noteworthy anomaly at 23 K suggests another magnetic transition [Fig. 4(b)]. We observed this anomaly in the PND but not in the single-crystal susceptibility measurements (see Fig. S3 in Supplemental Material [29]). As mentioned above, the magnetic transition at 23 K corresponds to  $\text{Mn}_3\text{TeO}_6$  in the polycrystalline sample. Another possible explanation for the 23-K feature might be linked to impurities from the grain

boundaries, which can contribute to the total magnetization. The magnetic structure of  $\text{Ni}_2\text{MnTeO}_6$  ceramics changes above 0.4 T [a double hysteresis loop is seen—Fig. 4(c)], and therefore the low-temperature anomaly in  $M(T)$  [Fig. 4(a)] disappears at higher fields.

Since pure  $\text{Ni}_3\text{TeO}_6$  exhibits a colossal static magnetoelectric coupling at the spin-flop transition near 8 T and a similar spin-flop transition occurs in  $\text{Ni}_2\text{MnTeO}_6$  4 T lower, pyrocurrent and capacitance measurements of  $\text{Ni}_2\text{MnTeO}_6$  crystals at external magnetic field are required. Unfortunately, the small size of our crystals did not allow such experiments. Growth of larger single crystals required for these experiments (more than 1 mm in diameter) is in progress.

#### D. Spin and lattice excitations

The IR reflectivity spectra of the  $\text{Ni}_2\text{MnTeO}_6$  ceramics for selected temperatures from 10 to 300 K are shown in Fig. 5(a), together with the fitted complex permittivity [Figs. 5(b) and 5(c)]. As predicted by the factor-group analysis for the  $R3$  structure, nine  $E(x, y, x^2 - y^2, xy, xz, yz)$  and nine  $A(x^2 + y^2, z^2, z)$  modes are expected, both IR and Raman active, analogously to the  $\text{Ni}_3\text{TeO}_6$  case [15,35]. All 18 modes are clearly visible in the IR spectra up to 300 K. Similarly to  $\text{Ni}_3\text{TeO}_6$ , the phonon eigenfrequencies are practically unaffected by temperature changes, since the  $R3$  space group is preserved at all investigated temperatures. The damping of the modes slightly decreases upon cooling, as expected. A few of the mode frequencies lie close to the values of those reported for  $\text{Ni}_3\text{TeO}_6$  [15,35], most of them corresponding to the vibrations of the  $\text{TeO}_6$  octahedra [36]. The eigenfrequency values of the measured IR-active modes at 10 K, together with the respective damping and dielectric strength, are presented in Table I. For comparison, the previously published  $\text{Ni}_3\text{TeO}_6$  IR modes at 7 K by Skiadopoulou *et al.* [15] are also listed. The possible structural distortion at the AFM (and FE) transition at 67 K suggested by the anomaly in the permittivity data [Fig. 3(b)] should have only a negligible effect on the IR spectra.

In Figs. 5(b) and 5(c), permittivity  $\varepsilon'(\omega)$  and extinction coefficient  $k(\omega)$  spectra are displayed, respectively. Here we plot  $k(\omega)$  spectra because we are not sure whether the excitation seen below  $10\text{ cm}^{-1}$  contributes to permittivity or magnetic permeability. These spectra were extracted by fitting the IR reflectivity spectra of Fig. 5(a) and complex terahertz spectra (Fig. 6) by damped harmonic oscillators [Eqs. (1) and (2)]. The static permittivity obtained from the fits amounts to  $\sim 10$ , close to the value of  $\sim 11$  reported in the radio-frequency range for  $\text{Ni}_3\text{TeO}_6$  by Oh *et al.* [12]. The permittivity of our ceramics at 1 MHz [Fig. 3(b)] even exceeds 20, but it is probably enhanced by a contribution of interlayer barriers on grain boundaries, which are responsible for a Maxwell-Wagner contribution to the permittivity [37], dominant especially above 100 K.

The highly dense ceramics allowed micro-Raman studies with the possibility of focusing at a single grain, since the laser spot diameter ( $\sim 4\ \mu\text{m}$ ) was much smaller than the typical grain size of  $30\ \mu\text{m}$  (confirmed by scanning electron microscopy micrographs—see Fig. S1 in Supplemental Material [29]). The spectra were collected in the back-scattering geometry, in both parallel and crossed polarizations, at temperatures from 4 to

TABLE I. Frequencies of the IR-active modes in the  $\text{Ni}_2\text{MnTeO}_6$  ceramics at 10 K and Raman-active modes at 4 K, as obtained by fits of IR reflectivity with  $\varepsilon_\infty = 3.9$ . The low-frequency mode in the first line was identified in the terahertz spectra as a magnon. The first column corresponds to the IR mode frequencies of  $\text{Ni}_3\text{TeO}_6$  ceramics at 7 K from Skiadopoulou *et al.* [15]. The damping constants and dielectric strengths of the IR-active modes are also listed. The modes observed as weak in Raman spectra are marked by  $w$  in subscript. All Raman modes which are not IR active correspond to longitudinal optic modes. The theoretical frequencies obtained by first-principles calculations are also included, together with the assigned symmetry for each mode in the parentheses.

$\text{Ni}_3\text{TeO}_6$ [15]	$\text{Ni}_2\text{MnTeO}_6$				
	IR 7 K	IR 10 K			
$\omega_{\text{TO}}$ ( $\text{cm}^{-1}$ )	Calculations $\omega(\text{cm}^{-1})$	Raman 4 K $\omega(\text{cm}^{-1})$	$\omega_{\text{TO}}$ ( $\text{cm}^{-1}$ )	$\gamma_{\text{TO}}$ ( $\text{cm}^{-1}$ )	$\Delta\varepsilon$
16.2			7.9	1.3	0.04
32.4					
	168.0 (A)	164.6	163.1	5.8	0.12
185.0	195.4 (E)	185.5 <sub>w</sub>	189.2	28.5	0.34
	206.8 (A)	211.2	205.4	5.4	0.85
219.3	220.8 (E)		214.8	6.4	0.16
232.1	243.6 (A)		240.9	23.9	0.23
259.2	265.6 (E)	266.0	262.8	14.5	0.83
279.3	284.9 (E)		284.2	17.3	0.74
303.1	319.4 (E)	300.0	293.6	8.7	0.07
313.2	352.8 (A)	354.1 <sub>w</sub>	345.8	18.1	0.50
345.2	368.7 (E)	369.7	369.8	7.2	0.10
361.7	408.1 (A)	403.2	397.2	33.4	0.25
380.0	440.0 (A)		431.4	9.8	1.17
406.6	443.7 (A)	436.5	435.7	6.3	0.21
454.2	507.7 (E)	475.6	509.3	14.4	0.29
466.1		484.3			
516.5	546.8 (E)	501.6	518.7	17.1	0.31
536.6	555.3 (E)	538.0	525.5	5.5	0.01
		570.8 <sub>w</sub>			
597.1	587.1 (A)	590.6	590.6	24.6	0.09
661.2		603.4 <sub>w</sub>			
	663.4 (A)	681.0 <sub>w</sub>	653.9	17.7	0.27
		693.6			
		720.0 <sub>w</sub>			

300 K. Here, only the crossed polarized spectra are presented, since no significant differences between the two polarizations were observed, except for different intensity magnitudes. A plot of the Raman spectra at selected temperatures from 4 to 300 K is shown in Fig. 5(d). The Raman mode frequencies at 4 K are presented in Table I in comparison with the IR modes at 10 K. The polycrystalline nature of the samples is not suitable for a symmetry analysis of the observed modes. All Raman modes which are not IR active correspond most probably to longitudinal optical modes (similarly as in  $\text{Ni}_3\text{TeO}_6$ —see Ref. [15]). As for the IR spectra, no substantial changes were observed on cooling, apart from splitting of the mode at around  $600\text{ cm}^{-1}$  and an expected decrease in damping. Such splitting originates mainly from the decrease in damping and a possible small frequency shift of the order of  $1\text{ cm}^{-1}$ , due to thermal contraction. No new modes due to a possible change of crystal

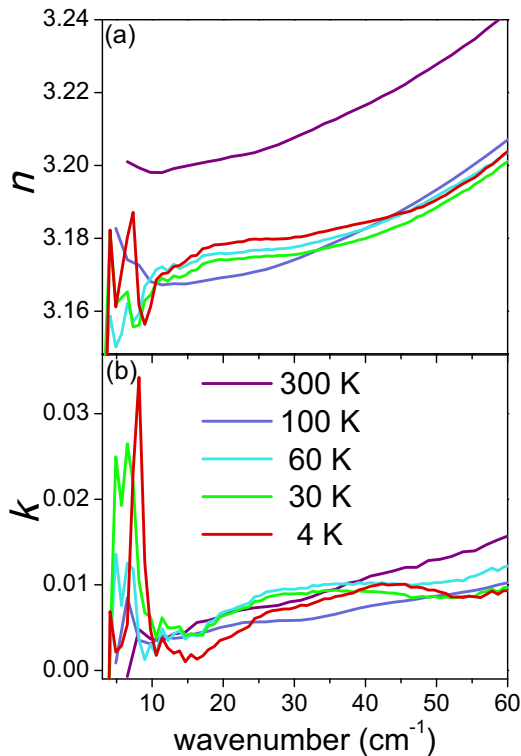


FIG. 6. Temperature dependence of the (a) real and (b) imaginary part of the complex index of refraction, obtained from terahertz time-domain spectroscopy.

symmetry, or due to appearance of spin excitations, activate below  $T_N$ . This absence of newly activated phonons in Raman and IR spectra below  $T_N$  supports the fact that the crystal symmetry is the same in the paramagnetic and ferromagnetic phases, belonging to the polar  $R3$  space group.

Lattice dynamics calculations, based on the computed Hellman Feynman forces, yield all expected 18 IR- and Raman-active phonon modes. The computed values are in good agreement with the experimental ones obtained by IR and Raman spectroscopies (see Table I).

Time-domain terahertz transmission measurements were performed for the  $\text{Ni}_2\text{MnTeO}_6$  ceramics (thickness 1.9 mm), at temperatures from 4 to 300 K. Figure 6 shows the terahertz spectra for selected temperatures. Upon cooling, a gradual decrease in the real part of the index of refraction occurs. The increase in  $n$  with frequency comes from the phonon contribution, and the value of  $n \approx 3.2$  is in agreement with the static permittivity value obtained from the IR spectra. A new low-frequency excitation at  $\sim 6 \text{ cm}^{-1}$  appears at 60 K, below the AFM transition of  $\sim 70 \text{ K}$ , and upon cooling it sharpens and shifts to  $8 \text{ cm}^{-1}$  at 4 K. Note that the signal is rather noisy below  $8 \text{ cm}^{-1}$ , since it is close to the border of the accessible frequency region. The emergence of the new excitation below the magnetic transition, in combination with the fact that all 18 phonons predicted by the factor-group analysis are resolved in the IR and Raman spectra, suggest that this new excitation is of magnetic origin. The broader feature, also notable at higher frequencies ( $\sim 40 \text{ cm}^{-1}$ ) in the  $k(\omega)$  spectra, and equally emerging below  $T_N$ , is possibly due to

multimagnon absorption. However, it may also correspond to a single-magnon excitation, since a similar feature at  $32 \text{ cm}^{-1}$  was observed in  $\text{Ni}_3\text{TeO}_6$ ; the high value of damping could be attributed to the chemical disorder of Mn in the lattice (PND revealed Mn in B sites of  $\text{A}_2\text{B}_2\text{O}_6$  with an occupancy rate of 93%, whereas 7% of B sites are occupied by Ni—see Table S1 in Supplemental Material [29]).

We measured terahertz spectra also in an external magnetic field of up to 7 T in the Voigt configuration, with  $\mathbf{H}_{\text{ext}}$  parallel and perpendicular to the electric vector  $\mathbf{E}^\omega$  of the terahertz beam. Here, we present only the spectra with  $\mathbf{H}_{\text{ext}} \perp \mathbf{E}^\omega$  (Fig. 7), where the magnetic-field effect upon the spin excitation was more pronounced (yet qualitatively the same). At 30 K [Fig. 7 (left)], the magnetic mode below  $10 \text{ cm}^{-1}$  shifts down and sharpens with increasing magnetic field. At 5 K [Fig. 7 (right)], a conspicuous sharpening up to 4 T takes place, followed by decrease in its intensity upon increasing  $\mathbf{H}_{\text{ext}}$  up to 7 T.

Such behavior might be related to the spin-flop transition occurring at around 4.5 T [Fig. 3(c)] or to the frequency limit of our experimental setup. Nevertheless, at 5 K a clear magnon frequency softening is exhibited with increasing  $\mathbf{H}_{\text{ext}}$ , from  $8 \text{ cm}^{-1}$  at 0 T to  $6 \text{ cm}^{-1}$  at 7 T.

Finally, the very small size of the single crystals did not allow for performing spectroscopic studies based on the orientation of the crystal structure. For example, directional dichroism might reveal the character of the spin excitation observed in the terahertz spectra and identify whether it corresponds to a pure magnon or electromagnon, as in  $\text{Ni}_3\text{TeO}_6$ . Unfortunately, since the magnetic excitation lies below  $8 \text{ cm}^{-1}$ , more precise transmission measurements with a spectrometer based on backward-wave oscillator sources [38] and a crystal with diameter at least 10 mm would be required. In addition, using single crystals, one can avoid possible impurities often present at grain boundaries of polycrystalline samples, thus the anomaly seen at 23 K could be absent or better resolved. Last but not least, capacitance and pyrocurrent measurements of  $\text{Ni}_2\text{MnTeO}_6$  single crystals in external magnetic field could shed more light on the magnetoelectric properties of  $\text{Ni}_2\text{MnTeO}_6$ , since the very similar compound  $\text{Ni}_3\text{TeO}_6$  presents a colossal magnetoelectric effect at the spin-flop transition occurring near 8 T.

#### IV. CONCLUSIONS

Single crystals and polycrystalline ceramic samples of the compound  $\text{Ni}_2\text{MnTeO}_6$  were synthesized. The Mn substitution of Ni in  $\text{Ni}_3\text{TeO}_6$  leads to an increase in the AFM transition temperature by 20 K, thus reaching  $\sim 70 \text{ K}$ , whereas the compound preserves the polar  $R3$  space group. At the same time, an anomaly is also seen in the low-frequency permittivity spectrum. Another anomaly observed at 23 K is likely due to a  $\text{Mn}_3\text{TeO}_6$  impurity phase. A spin-flop transition is triggered by an external magnetic field above 5 T, i.e.,  $\sim 3 \text{ T}$  lower than that of  $\text{Ni}_3\text{TeO}_6$ . Since in  $\text{Ni}_3\text{TeO}_6$  a colossal magnetoelectric effect close to the spin-flop transition is known to exist, a strong static magnetoelectric coupling in  $\text{Ni}_2\text{MnTeO}_6$  might appear at a lower magnetic field. To that aim growth of larger single crystals suitable for magnetoelectric studies is in progress.

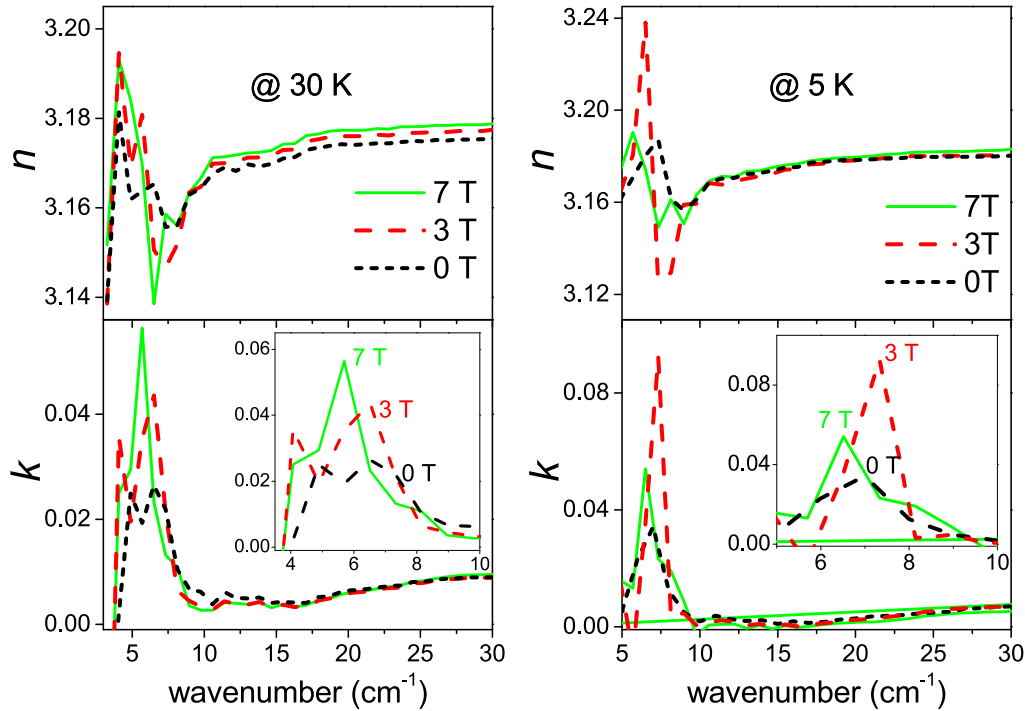


FIG. 7. Real and imaginary part of the index of refraction from the terahertz measurements of  $\text{Ni}_2\text{MnTeO}_6$  ceramics, at external magnetic field in Voigt configuration  $\mathbf{H}_{\text{ext}} \perp \mathbf{E}^\omega$ , for 30 K (left) and 5 K (right) as measured.

The high-quality dense ceramic samples revealed all expected IR- and Raman-active modes of the  $R3$  symmetry. A magnetic-field-tunable spin excitation at  $\sim 8 \text{ cm}^{-1}$  is clearly seen in the terahertz spectra below  $T_N$ . Such a low frequency of the magnon does not allow for measuring also its Raman spectra, leaving the question open whether the magnon bears a magnetoelectric character. Terahertz measurement of directional dichroism could reveal the character of the spin excitation (magnon or electromagnon). However, single crystals with more than 3 mm in diameter are required for such an experiment and these are not yet available.

#### ACKNOWLEDGMENTS

The work of M.G., M.R., and Z.D. was supported by NSF Grant No. DMR-1507252. M.R. also acknowledges the

Spanish Ministry of Economy and Competitiveness for the Juan de la Cierva Grant No. FPDI-2013-17582 and the Project No. ENE2016-77055-C3-3-R; and J.A.A. for the Project No. MAT2017-84496-R. The work of S.K., S.S., F.B., C.K., and F.K. was supported by European Union funding under the Seventh Framework Programme (Project NOTEDDEV), by the Czech Science Foundation (Projects No. 15-08389S and No. 18-09265S), and MŠMT KONTAKT II Project No. LH15122. EDS characterization of ceramics performed by K. Jurek is highly appreciated. D.L. and S.S. acknowledge the European Regional Development Fund in the IT4 Innovations national supercomputing centre—Path to Exascale (Project No. CZ.02.1.01/0.0/0.0/16\_013/0001791) within the Operational Programme Research, Development and Education, and D.L. acknowledges also Project No. 17-27790S of Czech Science Foundations and Mobility Grant No. 8X17046.

- [1] L. I. Kosse, E. D. Politova, V. V. Chechkin, E. A. Myzgin, Y. N. Medvedev, and B. S. Venetstseva, *Izv. Akad. Nauk SSSR, Neorg. Mater.* **18**, 1879 (1982).
- [2] L. I. Kosse, E. D. Politova, and Y. N. Venetstsev, *Zhurnal Neorganicheskoy Khimii* **28**, 1689 (1983).
- [3] M. Herak, H. Berger, M. Prester, M. Miljak, I. Zivkovic, O. Milat, D. Drobac, S. Popovic, and O. Zaharko, *J. Phys. Condens. Matter* **17**, 7667 (2005).
- [4] K. Y. Choi, P. Lemmens, E. S. Choi, and H. Berger, *J. Phys. Condens. Matter* **20**, 505214 (2008).
- [5] M. Hudl, R. Mathieu, S. A. Ivanov, M. Weil, V. Carolus, T. Lottermoser, M. Fiebig, Y. Tokunaga, Y. Taguchi, Y. Tokura, and P. Nordblad, *Phys. Rev. B* **84**, 180404 (2011).
- [6] S. A. Ivanov, P. Nordblad, R. Mathieu, R. Tellgren, C. Ritter, N. V. Golubko, E. D. Politova, and M. Weil, *Mater. Res. Bull.* **46**, 1870 (2011).
- [7] S. A. Ivanov, R. Tellgren, C. Ritter, P. Nordblad, R. Mathieu, G. Andre, N. V. Golubko, E. D. Politova, and M. Weil, *Mater. Res. Bull.* **47**, 63 (2012).
- [8] R. Mathieu, S. A. Ivanov, P. Nordblad, and M. Weil, *Eur. Phys. J. B* **86**, 1 (2013).
- [9] S. A. Ivanov, R. Mathieu, P. Nordblad, R. Tellgren, C. Ritter, E. Politova, G. Kaleva, A. Mosunov, S. Stefanovich, and M. Weil, *Chem. Mater.* **25**, 935 (2013).
- [10] M.-R. Li, D. Walker, M. Retuerto, T. Sarkar, J. Hadermann, P. W. Stephens, M. Croft, A. Ignatov, C. P. Grams, J. Hemberger,

- I. Nowik, P. S. Halasyamani, T. T. Tran, S. Mukherjee, T. S. Dasgupta, and M. Greenblatt, *Angew. Chemie Int. Ed.* **52**, 8406 (2013).
- [11] M.-R. Li, M. Retuerto, D. Walker, T. Sarkar, P. W. Stephens, S. Mukherjee, T. S. Dasgupta, J. P. Hodges, M. Croft, C. P. Grams, J. Hemberger, J. Sánchez-Benítez, A. Huq, F. O. Saouma, J. I. Jang, and M. Greenblatt, *Angew. Chemie Int. Ed.* **53**, 10774 (2014).
- [12] Y. S. Oh, S. Artyukhin, J. J. Yang, V. Zapf, J. W. Kim, D. Vanderbilt, and S.-W. Cheong, *Nat. Commun.* **5**, 3201 (2014).
- [13] J. W. Kim, S. Artyukhin, E. D. Mun, M. Jaime, N. Harrison, A. Hansen, J. J. Yang, Y. S. Oh, D. Vanderbilt, V. S. Zapf, and S.-W. Cheong, *Phys. Rev. Lett.* **115**, 137201 (2015).
- [14] X. Wang, F.-T. Huang, J. Yang, Y. S. Oh, and S.-W. Cheong, *Appl. Mater.* **3**, 76105 (2015).
- [15] S. Skiadopoulou, F. Borodavka, C. Kadlec, F. Kadlec, M. Retuerto, Z. Deng, M. Greenblatt, and S. Kamba, *Phys. Rev. B* **95**, 184435 (2017).
- [16] M.-R. Li, M. Croft, P. W. Stephens, M. Ye, D. Vanderbilt, M. Retuerto, Z. Deng, C. P. Grams, J. Hemberger, J. Hadermann, W.-M. Li, C.-Q. Jin, F. O. Saouma, J. I. Jang, H. Akamatsu, V. Gopalan, D. Walker, and M. Greenblatt, *Adv. Mater.* **27**, 2177 (2015).
- [17] G. Bayer, *Zeit. Krist.* **124**, 131 (1967).
- [18] H. G. Burckhardt, C. Platte, and M. Trömel, *Acta Crystallogr. Sect. B* **38**, 2450 (1982).
- [19] J. A. Baglio and S. Natansohn, *J. Appl. Crystallogr.* **2**, 252 (1969).
- [20] R. Becker, M. Johnsson, and H. Berger, *Acta Crystallogr. Sect. C* **62**, i67 (2006).
- [21] A. Hostachy and J. Coing-Boyat, *C. R. Acad. Sci.* **267**, 1425 (1968).
- [22] H. M. Rietveld, *J. Appl. Crystallogr.* **2**, 65 (1969).
- [23] J. Rodríguez-Carvajal, *Physica B* **192**, 55 (1993).
- [24] F. Gervais, in *High-Temperature Infrared Reflectivity Spectroscopy by Scanning Interferometry Vol. 8: Infrared Millimeter Waves*, edited by K. J. Button (Academic, New York, 1983), Chap. 7, p. 279.
- [25] M. Tyunina, A. Dejneka, D. Rytz, I. Gregora, F. Borodavka, M. Vondracek, and J. Honolka, *J. Phys. Condens. Matter* **26**, 125901 (2014).
- [26] G. Kresse and J. Furthmüller, *Phys. Rev. B* **54**, 11169 (1996).
- [27] J. P. Perdew, K. Burke, and M. Ernzerhof, *Phys. Rev. Lett.* **77**, 3865 (1996).
- [28] S. L. Dudarev, G. A. Botton, S. Y. Savrasov, C. J. Humphreys, and A. P. Sutton, *Phys. Rev. B* **57**, 1505 (1998).
- [29] See Supplemental Material at <http://link.aps.org/supplemental/10.1103/PhysRevB.97.144418> for supplemental figures and tables.
- [30] R. Becker and H. Berger, *Acta Crystallogr. Sect. E* **62**, 222 (2006).
- [31] I. Živković, K. Prša, O. Zaharko, and H. Berger, *J. Phys. Condens. Matter* **22**, 056002 (2010).
- [32] L. Zhao, Z. Hu, C.-Y. Kuo, T.-W. Pi, M.-K. Wu, L. H. Tjeng, and A. C. Komarek, *Phys. Status Solidi: Rapid Res. Lett.* **9**, 730 (2015).
- [33] S. A. Ivanov, C. Ritter, P. Nordblad, R. Tellgren, M. Weil, V. Carolus, T. Lottermoser, M. Fiebig, and R. Mathieu, *J. Phys. D* **50**, 085001 (2017).
- [34] Y. Tokura, S. Seki, and N. Nagaosa, *Reports Prog. Phys.* **77**, 076501 (2014).
- [35] M. O. Yokosuk, S. Artyukhin, A. Al-Wahish, X. Wang, J. Yang, Z. Li, S.-W. Cheong, D. Vanderbilt, and J. L. Musfeldt, *Phys. Rev. B* **92**, 144305 (2015).
- [36] G. Blasse and W. Hordijk, *J. Solid State Chem.* **5**, 395 (1972).
- [37] P. Lunkenheimer, S. Krohns, S. Riegg, S. G. Ebbinghaus, A. Reller, and A. Loidl, *Eur. Phys. J. Spec. Top.* **180**, 61 (2009).
- [38] A. Shuvaev, V. Dziom, A. Pimenov, M. Schiebl, A. A. Mukhin, A. C. Komarek, T. Finger, M. Braden, and A. Pimenov, *Phys. Rev. Lett.* **111**, 227201 (2013).